

Lightweight Embedded FPGA Deployment of Learned Image Compression with Knowledge Distillation and Hybrid Quantization

Mazouz Alaa Eddine  ¹, Sumanta Chaudhuri  ¹, Attilio Fiandrrotti  ^{3,1}, Marco Cagnazzo  ¹, Mihai Mitrea  ², and Enzo Tartaglione  ¹

¹LTCI, Télécom Paris, Institut Polytechnique de Paris, France

²SAMOVAR, Télécom SudParis, Institut Polytechnique de Paris, France

³Università di Torino, Italy

Email: alaa.mazouz@telecom-paris.fr

Abstract—Learnable Image Compression (LIC) has shown the potential to outperform standardized video codecs in RD efficiency, prompting the research for hardware-friendly implementations. Most existing LIC hardware implementations prioritize latency to RD-efficiency and through an extensive exploration of the hardware design space. We present a novel design paradigm where the burden of tuning the design for a specific hardware platform is shifted towards model dimensioning and without compromising on RD-efficiency. First, we design a framework for distilling a leaner student LIC model from a reference teacher: by tuning a single model hyperparameters, we can meet the constraints of different hardware platforms without a complex hardware design exploration. Second, we propose a hardware-friendly implementation of the Generalized Divisive Normalization - GDN activation that preserves RD efficiency even post parameter quantization. Third, we design a pipelined FPGA configuration which takes full advantage of available FPGA resources by leveraging parallel processing and optimizing resource allocation. Our experiments with a state of the art LIC model show that we outperform all existing FPGA implementations while performing very close to the original model.

Keywords—FPGA, Deep Learning, Learned Image Compression, Autoencoder, Quantization, Pruning, Knowledge Distillation.

I. INTRODUCTION

Learned Image Compression (LIC) [1] replaces traditional coding tools in standardized codecs with an end-to-end learnable autoencoder-based model. First, the image is projected into a low-dimensional latent space by the encoder. This representation is then quantized and entropy-coded into a binary bitstream. At the receiver end, the bitstream is entropy-decoded, and the decoder recovers an approximation of the original image from the latent representation. While adding uniform noise during training helps cope with the non-differentiability of quantization, the Generalized Divisive Normalization (GDN) activation minimizes mutual information in the latent space, improving RD efficiency. To date, LIC outperforms early still-image standards such as JPEG and JPEG2000 and performs on par with the intra profile of recent standards such as H.266/VVC.

While research on LIC largely focused on enhancing RD efficiency through improved architectures [2], [3], [4], [5], [6], quantization-entropy coding stages [7], [8], [9], [10], the implications of hardware implementations are frequently overlooked. In low-power, embedded/mobile devices, hardware accelerators (FPGA/ASIC) are crucial for meeting latency targets in Frames Per Second (FPS) while meeting power and complexity constraints. Addressing real-time latency demands involves optimizing computational [11] and power efficiency [12], [13], [14], ensuring cross-platform support [15], and compatibility with edge computing devices [14] [16]. Hardware-aware design strategies, such as model pruning [17], [18], and fixed-point parameter quantization [19], are essential tools for bridging the gap between algorithmic design and hardware implementation in any applicative domain.

State-of-the-art hardware LIC implementations like [20], [21], [22] are highly hardware-efficient and can achieve real-time latency (in the case of [22]) by leveraging advanced design techniques and optimizing DSP efficiency. However, such design techniques imply a deep understanding of the specific hardware platform the implementation is designed for and a time-consuming exploration of the design space to meet a latency deadline. Also, real-time operations are often achieved at the expense of RD performance, resulting in significant drops when the hardware implementation is compared to the original LIC model it is based upon. Such drawbacks have prompted our research, where we aim to balance hardware and software optimization by adopting design choices at all levels while ensuring that real-time hardware operations do not come at the expense of RD efficiency by designing ad-hoc components.

The main contributions of this work can be summarized as follows.

- **Latency model:** We analytically model the relationship between the number of convolutional channels of a LIC architecture and its latency in terms of FPS. Showing that computational complexity dominates this relationship, we derive an upper bound to latency that is sufficient to dimension the convolutional layers' width to meet a target

frame rate.

- **Knowledge Distillation:** We design a framework for distilling a reference LIC teacher model into a smaller student with fewer convolutional channels while keeping the RD efficiency close to the reference. To the best of our knowledge, our work is the first to leverage knowledge distillation to train smaller LIC models suitable for embedded deployment.
- **GDN Implementation:** We introduce an implementation of the Generalized Divisive Normalization layer that is hardware-friendly yet preserves RD efficiency when the LIC model is deployed on FPGA. This is a major departure from the approach by Sun et al. [22], where the GDN is replaced with a simpler ReLU to improve latency.
- **Hybrid Quantization-Aware Training (QAT) and Pruning:** We introduce a hybrid QAT-based pruning method, which outperforms Post-Training Quantization (PTQ) in terms of RD efficiency. This approach, combined with mixed precision (MP) for the GDN layers, enhances the model’s RD performance while maintaining hardware efficiency. We also propose a structured pruning approach that optimizes model size and latency, contributing to better resource utilization and lower latency on FPGA.
- Finally, we present a fully pipelined architecture that maximizes hardware resource utilization.

Our experiments show state-of-the-art results in terms of latency, energy efficiency, and resource utilization on the ZCU102 FPGA board (Fig.9 and Table IV). We also outperform state-of-the-art competitors in terms of RD efficiency, i.e., we enable video quality better than other hardware LIC methods despite the better latency. Most importantly, our approach allows meeting different target frame rates without requiring a complex exploration of the hardware design space.

The outline of this paper is as follows. Section II introduces the required background on LIC and discusses the limits of existing hardware implementations. Section III introduces our proposed design methodology involving knowledge distillation, pruning, quantization, and hardware pipelining. Finally, Section IV provides experimental results for the hardware-implemented models on the ZCU102 boards in terms of RD efficiency, latency, power consumption, and resource utilization. In Section IV-D, an in-depth ablation study of each key component of the proposed architecture quantifies the contribution of each component to our overall gains.

II. BACKGROUND AND RELATED WORKS

In this section, we first provide the relevant background on Learned Image Compression (LIC). Then, we overview the existing approaches to hardware friendly LIC, highlighting existing limitations that motivate our work.

A. A primer on Learned Image Compression

Learned Image Compression (LIC) has demonstrated the ability to match or even outperform standardized codecs in terms of rate-distortion (RD) performance. Foundational

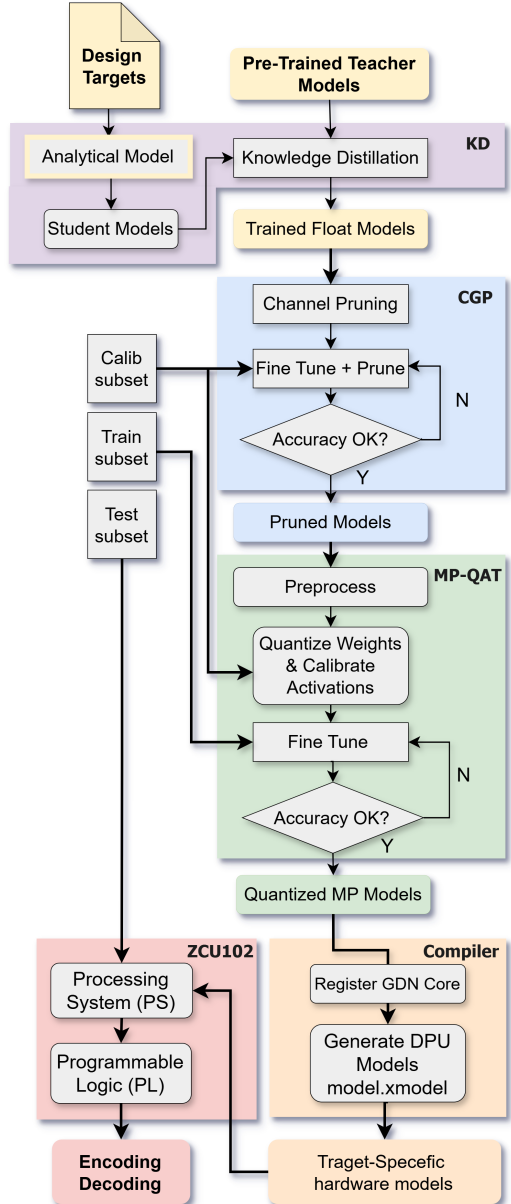


Fig. 1: Overall proposed workflow for embedded LIC

works, such as those by Ballé et al [2] and Theis et al. [23] leveraged a simpler convolutional autoencoder architecture. At the transmitter side, a convolutional encoder g_a preliminary compresses the image x projecting it onto a low-dimensional hidden latent space y (*nonlinear analysis* coding). The latent space elements are quantized adding uniform noise at learning time to mimic the rounding operation as a proxy of the non differentiable quantization. The quantized hidden space \tilde{y} is then entropy coded and put on the wire as a binary bitstream. In early works, the probability of each i -th element \tilde{y}_i of the latent space is learned at training time (*fully factorized*) without any assumption on the underlying distribution shape (*non-parametric*). At the receiver side, the bitstream is entropy-decoder and a convolutional decoder g_s recovers an approximation \tilde{x} of the original image (*nonlinear synthesis*). The model is optimized end-to-end by backpropagating and

descending the error gradient to minimize the cost function

$$L = R + \lambda \cdot D,$$

where λ adjusts the trade-off between the rate of the compressed bitstream and the distortion D of the reconstructed image. The rate R of the latent space is estimated by an auxiliary ad-hoc neural network. The distortion between the original image x and the decoded image \tilde{x} is measured either in Mean Squared Error (MSE) terms or perceptually via the Structural Similarity Index (SSIM).

The model relies on the Generalized Divisive Normalization (GDN) [24] activation at the encoder side (and relative inverse GDN at the decoder side). The GDN activation Gaussianizes the latent space y reducing the mutual information amongst components, improving the compression efficiency over the ubiquitous ReLU-like activations used for hidden layers [9]. Such scheme outperformed the JPEG and JPEG2000 standards despite the relatively simple entropy model it relies upon.

The above scheme was improved in [3] introducing a secondary latent space known as the *hyperprior*. Rather than learning the distributions of the latents y at training time, they are now predicted for each encoded image exploiting the fact that the scale θ of neighbor components usually varies jointly. The hyperprior latent representation z is first quantized using a factorized entropy model and delivered to the receiver within the bitstream. The main quantized latent space \hat{y} is then entropy coded assuming a Gaussian distribution with $\mu = 0$ and using the scales recovered by the hyperprior decoder available also to the receiver. The model can still be trained end-to-end yet simply adding to the cost function the estimated entropy of the hyperprior. Despite the burden of delivering the compressed hyperprior as side information, such scheme performs en pair with the H.265/HEVC Intra profile (BPG). Clearly, this scheme is more complex due to the presence of hyper encoder and decoder, that are in turn implemented as a nested convolutional autoencoder with GDN normalization.

The works in [25], [7] combined previous architectures with a context-based auto-regressive entropy model to capture more local spatial correlation by exploiting already decoded parts of images. A scheme of this approach is partially presented in Fig. 2, while [26] introduced channels-block decoding and performed block-based encoding to exploit the already decoded part of the latent representation. In more recent works other techniques have been exploited to improve RD performance; [8] replaced simple Gaussian distribution with a mixture of Gaussians and introduced an attention module to enhance entropy estimation. In [27] local attention is exploited to combine the local-aware attention with the global-related feature learning and to date, it remains among the best-performing architectures. We selected this work simply because it represents one of the most recent ones that subsequent works have built upon;

At this point, we note that the existing literature on hardware-friendly implementations has mostly explored CNN-based models due to the difficulty of implementing in HW transformer modules. Additionally, the existing literature has particularly explored [25] as it offers good RD performance

and HW efficiency as well and that's also why in our work we focus on this model rather than on more modern models. At this point we review notable implementations of this model like [20], [22] saying that they achieve realtime operations yet at the expense of RD performance and how, especially the lack of GDN. We conclude that the lack of LIC hardware solution that is both hardware friendly and RD performing motivates our work.

The literature on hardware-friendly image compression (LIC) models is sparse, with existing works predominantly focusing on CNN-based approaches rather than Transformer-based models. This is largely due to the inherent challenges of efficiently implementing Transformer modules in hardware. Among CNN-based models, [22] stands out for building upon [21] and achieving an effective balance between rate-distortion (RD) performance and hardware efficiency, making it the current state of the art in the field. Consequently, our work adopts this model rather than more modern architectures. Notable hardware implementations, such as [22] and [21], have demonstrated real-time processing capabilities but often at the cost of RD performance. These limitations stem from the absence of Generalized Divisive Normalization (GDN) layers and reliance on computationally intensive architectures from the literature. Additionally, [20] targets high-resolution deployment, achieving 4K video decoding, though at frame rates significantly below real-time requirements. The current lack of a hardware solution for LIC that simultaneously delivers hardware efficiency and superior RD performance underscores the motivation for our work, which seeks to develop novel techniques to effectively train and deploy computationally intensive LIC models for real-time applications. In [28]A hierarchical VAE architecture, originally designed for generative image modeling, is utilized for LIC, redefining their probabilistic model to allow easy quantization and practical entropy coding.

TABLE I: Components and Symbols for the Hyperprior LIC model

Component	Symbol
Input Image	x
Encoder	$f(x; \theta_e)$
Latents	y
Latents (quantized)	\hat{y}
Latents (quantized, student)	\hat{y}_s
Latents (quantized, teacher)	\hat{y}_t
Decoder	$g(\hat{y}; \theta_d)$
Hyper Encoder	$f_h(y; \theta_{he})$
Hyper-latents	z
Hyper-latents (quantized)	\hat{z}
Hyper Decoder	$g_h(\hat{z}; \theta_{hd})$
Context Model	$g_{cm}(y_{<i}; \theta_{cm})$
Entropy Parameters	$g_{ep}(\cdot; \theta_{ep})$
Reconstruction	\hat{x}
Reconstruction (student)	\hat{x}_s
Reconstruction (teacher)	\hat{x}_t

III. PROPOSED METHOD

In this section, we introduce our proposed method consisting in a initial knowledge distillation from a large teacher to a smaller student. Next, the student is implemented using a

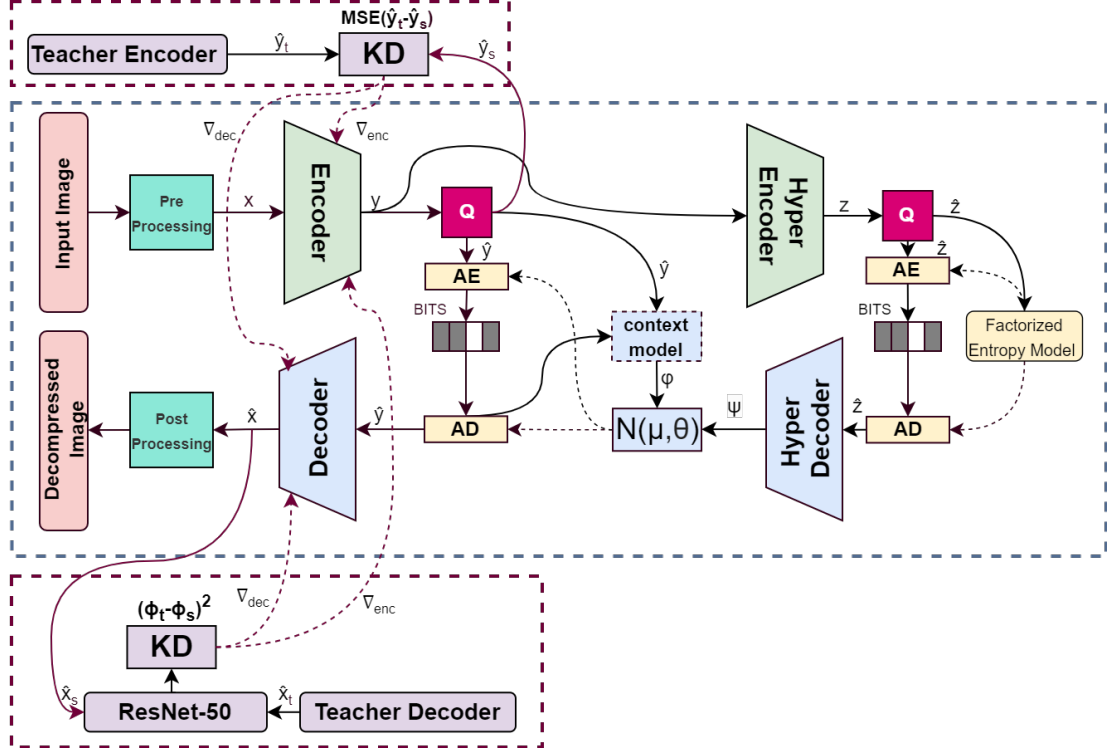


Fig. 2: Hyper-prior models capture broader image features, while context entropy model looks at the already decoded neighboring pixels (the causal context) and predicts the distribution of the next pixel based on that context

hardware-friendly GDN/iGDN implementation, the model is pruned, quantized and finally deployed on hardware.

A. Knowledge Distillation for LIC

This section proposes a Knowledge Distillation (KD) strategy to teach a *student* LIC model from a larger reference *teacher*. We first propose a straightforward strategy to dimension a student model with lower complexity than a reference teacher and then we discuss the procedure to distill knowledge from the teacher and into the student.

1) *Designing and training a student model:* We recall that, given a reference LIC model, our ultimate goal is to deploy it on some hardware platform while meeting some target latency. In approaches like [SUN24], the model complexity is cut by altering its topology (e.g., replacing the GDN activations with RELUs) and via a thorough exploration of the hardware design space. However, altering the model topology badly impacts its RD-efficiency, whereas exploring the hardware design space can be a time-consuming activity. We point out that in models like [3], the main source of complexity lies in the filtering operations performed by the convolutional layers. Multiple hyperparameters drive such complexity, including the number of layers, number of channels per layer, filter sizes, down-sampling strategies, etc. Our approach consists in controlling the model complexity by reducing the number of channels per convolutional layer without altering the model topology otherwise. Indeed, exploring one single model hyperparameter is way simpler than exploring the multiple options available in the hardware design space. Also, this approach aligns with established practices in the LIC literature, where reducing

channels is commonly used to create smaller, more computationally efficient models [3], [9]. Therefore, we initially design a lower-complexity student model that has a fraction of the number of channels of the reference model. Makes exception to this design rule the dimensions of the last convolutional layer of each encoder and decoder so to preserve the latent spaces dimensions. Preserving the latent spaces dimensions is key for distilling knowledge from the teacher, as discussed below. The student main-model parameters are initialized at random while the student hyperprior model utilizes the teacher's hyperprior, the student is trained minimizing the same $\mathcal{L}_{\text{initial}} = \mathcal{R} + \lambda \mathcal{D}$ loss function over the same training set. However, such student is less RD-efficient than the reference, as we experimentally show later on. Therefore knowledge must be distilled into the student from the reference model that acts as a teacher, as discussed below.

2) *Fine-tuning the student:* After designing and preliminarily training the student as above, knowledge is distilled from the teacher to recover the lost RD-efficiency. The dotted boxed in Fig.2 shows how our KD strategy plugs in the training of our reference LIC model. In detail, the student is fine-tuned by minimizing the following loss function

$$\mathcal{L}_{\text{KD}} = \alpha \mathcal{L}_{\text{latent}} + \beta \mathcal{L}_{\text{perc}} + \gamma (\mathcal{R} + \lambda \mathcal{D}), \quad (1)$$

where the various terms are as follow. The latent space loss term $\mathcal{L}_{\text{latent}}$ measures the distance between the teacher's (\mathbf{z}_t) and the student's latent representations (\mathbf{z}_s) as $\mathcal{L}_{\text{latent}} = \text{MSE}(\mathbf{z}_t, \mathbf{z}_s)$. This loss term drives the student to produce latent representations of the input image that match those of

the teacher.

The perceptual loss term $\mathcal{L}_{\text{perc}}$ measures instead the difference between the images decoded by the teacher (\mathbf{x}_t) and the student (\mathbf{x}_s). It consists of a perceptual loss computed by comparing feature maps extracted from specific layers of a pre-trained ResNet-50 model as

$$\mathcal{L}_{\text{perc}} = \sum_{i \in \{3,4,5\}} \|\phi_i(\mathbf{x}_t) - \phi_i(\mathbf{x}_s)\|^2, \quad (2)$$

where $\phi_i(\mathbf{x})$ denotes the feature map of the reconstructed image \mathbf{x} at layer i . The perceptual loss encourages the student model to focus on higher-level semantic similarities between images, rather than merely pixel-wise similarity. Layers 3, 4, and 5 of ResNet-50 are selected as they correspond to increasingly abstract feature representations, progressively moving from edges and textures to object structures. Namely, Layer 3 captures low-level features like edges and textures, essential for preserving fine details in compression. Layer 4 captures mid-level features such as object parts, crucial for maintaining structural coherence. Finally, Layer 5 captures high-level features, representing more abstract and semantic information, essential for preserving the perceptual quality of the image.

Finally, the third term in the loss function is the same RD cost term used to preliminary train the student. During fine-tuning, the three terms of the loss function loss weights α, β, γ are dynamically adjusted as follows. Early on during fine-tuning, α is set to 1.0 and β is set to 0.1 to drive the student latent space to match the teacher latent space and thus achieve similar latent space entropy. Later on, α is reduced to 0.1 and β is increased to 1.0 to promote visual quality. The transition between the early and late phases is automated by monitoring the performance plateaus. For instance, once the latent space loss $\mathcal{L}_{\text{latent}}$ stabilizes, the weights are automatically adjusted to emphasize the output space. Empirically, the number of training epochs for each phase can be set to 500 each which meets all the requirements we've outlined here on our chosen dataset. The γ weight is set to 0.5 throughout the distillation to maintain balance with the RD loss and avoid catastrophic forgetting of the original end-to-end compression task. Table II in the experimental section provides all the relevant hyperparameters for the distillation process. It is worth mentioning that throughout the training the initially trained teacher hyperprior model is being reused.

TABLE II: Hyperparameters for the KD Training Scheme

Hyperparameter	Initial Training	Fine Tuning	
		Early	Late
Learning Rate	1e-3	1e-4	1e-6
Decay [Step, Rate]	500k, 0.95	250k, 0.9	250k, 0.9
Batch Size [256x256]	16	8	8
α	NA	0.1	1.0
β	NA	1.0	0.1
γ	NA	0.5	0.5
Steps	5M	2.5M	2.5M
λ	0.0016, 0.0032, 0.0075, 0.045		

B. Efficient GDN design for FPGA implementation

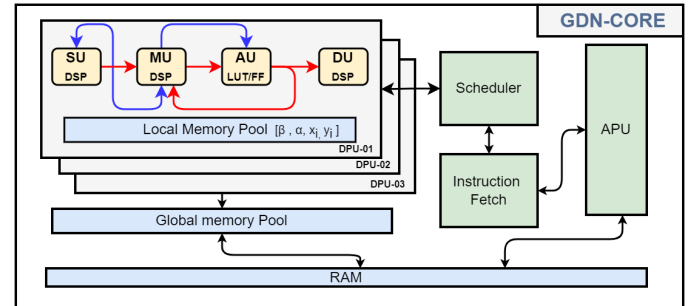


Fig. 3: Custom GDN/iGDN core integration, red for GDN, blue for iGDN pipeline using Square Unit, Multiply Unit, Add Unit and Division Unit

Other works [20], [21], [22] replace the GDN layer with ReLU activation to simplify the implementation. For our FPGA-based LIC architecture, we are the first to propose a custom Generalized Divisive Normalization (GDN) hardware engine to optimize RD performance. The GDN layer is essential for reducing statistical dependencies between activations in LIC models, which improves compression quality. Given an input feature map $\mathbf{x} \in \mathbb{R}^{H \times W \times C}$, where H , W , and C are the height, width, and number of channels respectively, the GDN operation is defined as:

$$y_i = \frac{x_i}{\left(\beta_i + \sum_j \gamma_{ij} x_j^2\right)^\alpha} \quad (3)$$

Where:
- y_i is the normalized output,
- x_i is the input activation from channel i ,
- β_i is a learned bias parameter ensuring positive output,
- γ_{ij} is a learned parameter controlling the interaction between different channels,
- α is a parameter controlling the non-linearity, typically fixed to 0.5.

In the decoder side, the inverse GDN (iGDN) operation is used, defined as:

$$x_i = y_i \left(\beta_i + \sum_j \gamma_{ij} y_j^2 \right)^\alpha \quad (4)$$

To efficiently implement the GDN layer on FPGA, we decomposed the mathematical operations into hardware-optimized components, leveraging the inherent parallelism and resource flexibility of the FPGA. First, the element-wise squaring operation is mapped directly onto DSP slices, which are well-suited for fast multiply-and-accumulate (MAC) operations. This minimizes latency and ensures high throughput for squaring, which is crucial given the dense computation of the GDN normalization. The division operations, critical for computing normalized activations, are also assigned to DSP slices but are carefully pipelined to ensure a continuous flow of data. By using a reciprocal approximation technique, we reduce the complexity of the division operation, converting it into a more efficient multiplication that fits within the limited

FPGA resources without compromising on accuracy. For the weighted summation of the normalization, we utilize BRAMs (Block RAM) to store intermediate results and parameters. BRAM offers low-latency access to these values, ensuring that the summation step remains efficient even as the size of the feature maps scales up. By distributing the BRAM across multiple FPGA regions, we further enhance parallelism and enable multiple summation operations to occur concurrently across different regions of the GDN layer. The exponentiation step, which involves computing the square root, is handled using a custom LUT-based approach. Instead of relying on traditional arithmetic units, which would significantly increase the resource usage, we implemented a piecewise-linear approximation of the square root function. This approximation is stored in LUTs, enabling rapid lookups during execution. The precision of this LUT-based approach is adjustable, allowing for dynamic trade-offs between accuracy and resource consumption based on application needs.

Given the quantization sensitivity of the GDN layer, especially in its non-linear components, we designed a custom mixed-precision quantization strategy. While the rest of the neural network uses lower-precision 8-bit fixed-point representation for weights, activations, and biases, the GDN layer operates with 32-bit fixed-point precision for its core calculations. This ensures that the precision loss introduced by quantization does not adversely impact the rate-distortion performance of the overall model. The fixed-point operations for GDN are meticulously tuned to balance the accuracy-resource trade-off, ensuring minimal degradation in model quality while optimizing FPGA resource usage, especially with regards to DSP slices and BRAM. The integration into the Vitis AI [29] environment required custom extensions to the Xilinx Intermediate Representation (XIR). We registered the GDN layer as a custom operation within the XIR framework, enabling the Vitis AI compiler to offload the GDN computations to a specialized Deep Processing Unit (DPU) core rather than relying on the embedded CPU. By synchronizing the GDN layer's input-output buffers with those of the other xmodel runners, the DPU can operate with the rest of the model pipeline. This setup, as illustrated in Fig.4.

The custom GDN layer is integrated into the FPGA workflow by registering it as an operation within the Vitis AI framework, as shown in Fig.4. The process begins by creating the graph runner with `create_graph_runner()`, followed by allocating input and output tensor buffers via `get_input/output_tensor_buffers()`. These buffers are synchronized with the FPGA memory using `input->sync_for_write()` before execution. The GDN operation is performed asynchronously using `execute_async(input_tensor_buffers, output_tensor_buffers)`, which offloads computation to the DPU. Once the operation is completed, the result buffers are synchronized back with `output->sync_for_read()`, and postprocessing is applied via `postprocess_GDN_op()`. This flow ensures efficient integration of the GDN layer, allowing it to run on the DPU in parallel with other operations, optimizing resource use and minimizing latency.

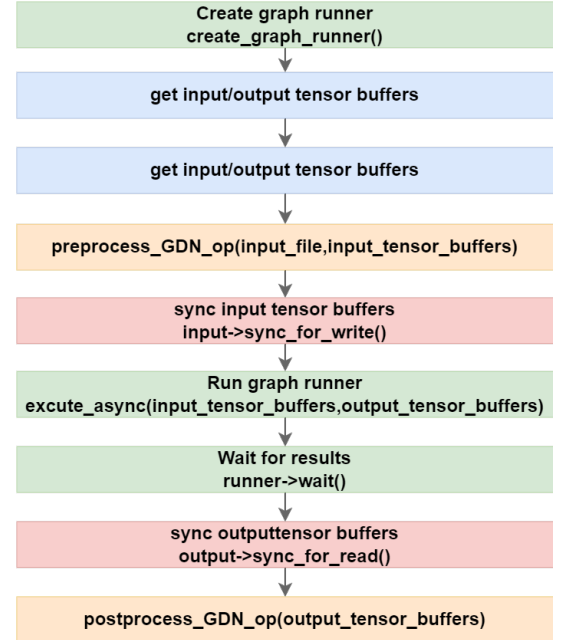


Fig. 4: Registering the custom GDN core with the XIR

C. Channel pruning

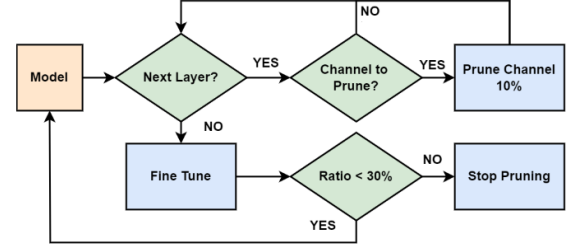


Fig. 5: The model is iteratively pruned 10% of its filters in three iterations until 30% sparsity is achieved, fine-tuning restoring the lost RD-efficiency.

Neural networks need to be over-parameterized to be successfully trained, so we prune the student LIC model to learn a sparse network topology and reduce FLOPs further. While unstructured pruning (i.e., pruning single weights) has the potential to achieve higher sparsity, the DPU instructions are not designed to deal with parameter-level sparsity. Channel pruning is instead more hardware-friendly and can be implemented with most inference architectures, most importantly with Xilinx DPU compilation instructions [30]. Fig. 5 (overall diagram-blue box) details the iterative prune-and-finetune procedure. We shoot for pruning 30% of the convolutional filters across three pruning iterations. The initial input to the procedure is the student model refined as described above. At each iteration and for each layer, 10% of the filters with lowest L2 magnitude are pruned from the model. If a neuron is left without filters, the entire neuron is pruned from the layer. As pruning filters impairs the model RD-efficiency, the model is fine-tuned until the previous performance is restored. This procedure is repeated three times until a 30% filter

level sparsity is achieved. We found that this iterative pruning strategy enables better sparsity-performance tradeoff than single-pass pruning. The filter pruning ratio directly affects the computational complexity as $\text{FLOPs}(\text{pruned model}) = (1 - \text{ratio}) \times \text{FLOPs}(\text{original model})$. We will explore the the improvements gained by pruning the model, most notably the significant reduction in latency, model size and FLOPs in the experimental section.

D. Mixed precision quantization

The parameters that survived pruning are then quantized towards integers arithmetic operations over FPGA. In most hardware LIC implementations, all parameters are pruned over 8-bit precision to minimize latency. Conversely, we proposed a mixed-precision quantization scheme where different model components are assigned different bit numbers. Specifically, the Generalized Divisive Normalization (GDN) layer is assigned a higher precision of 32-bit, while the rest of the model operates at 8-bit precision. This decision is motivated by the fact that the GDN layer, while only responsible for approximately 4% of the total FLOPS in the model, plays a critical role in improving the RD efficiency [31]. We recall that GDN’s primary function is to normalize activations across channels, promoting decorrelation in the latent space and improving RD efficiency. Lower precision (8-bit) introduces quantization noise in GDN’s operations such as division and normalization, which diminishes the accuracy of these transformations. By assigning 32-bit precision to the GDN layer, we reduce this quantization noise, leading to better normalization and decorrelation, ultimately enhancing rate-distortion performance, as we experimentally show also later on. Fig.6 illustrates the overall quantization strategy. Preliminarily, min and max values are extracted from the different model layers, allowing the quantizer to derive the optimal scale and zero point from the float model using the calibration subset. This subset includes 1000 random images from CLIC [32], DIV2K [33], and Open Images [34], used only for a forward pass. Symmetric quantization is achieved by setting the zero point to zero, with saturation applied to minimize quantization differences. As quantization impairs the model performance, the model undergoes a Quantization Aware Tuning (QAT) is then tuned again for 1000 iterations over a subset of 5000 images from CLIC, DIV2K, and Open Images. Simulated quantization operations are introduced on both weights and activations, except for the GDN layer, which maintains 32-bit precision to avoid losing the benefits of accurate normalization. During each forward pass, operations use the quantized weights and activations, and gradients are computed with respect to the quantized parameters using a Straight-Through Estimator (STE) [36] to approximate gradients through the quantization process. The outcome of the quantization process is an LIC model that exclusively relies on integer operations, meeting the requirements for efficient FPGA deployment.

E. Design Space Exploration

In this section, we finally describe the hardware configuration we use for implementing the quantized LIC model

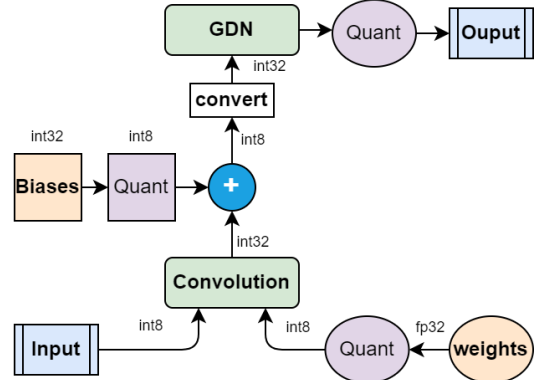


Fig. 6: Our mixed precision quantization strategy where GDN layers are quantized over 32 bits while the rest of the model is quantized over 8 bits.

model on FPGA using the Vitis AI platform [29]. Namely, we target the Xilinx ZCU102 FPGA that houses three DPU cores running at 300 MHz. We propose below a fully pipelined configuration employing the common B4096-DPU core configuration. Such configuration provides a peak of 4096 Multiply-Accumulate (MAC) operations per cycle featuring 16 input channels, 16 output channels, and processing 8 pixels per cycle. Namely, we seek a fully pipelined configuration where each of the three DPU cores operates in parallel, as depicted in Fig.7. By dividing the image into three patches sized 256×256 patches and processing multiple patches concurrently, the fully pipelined configuration optimizes resource utilization and minimizes end-to-end latency. Each DPU core handles a distinct patch, ensuring continuous processing and efficient use of the available computational resources. This setup dedicates each DPU to processing different image patches simultaneously, thereby maximizing throughput and reducing idle times.

The model is compiled into target-specific DPU instructions in the form of an xmodel. The XIR compiler constructs an internal computation graph as an intermediate representation (IR), it then performs multiple optimizations, such as computation node fusion, and efficient instruction scheduling by exploiting inherent parallelism or exploiting data reuse on the specific target. This unified IR is broken down into subgraphs based on the corresponding control flow, for our models multiple DPU subgraphs are compiled as the custom GDN layers require separate graphs. Finally, an instruction stream is generated for each subgraph and everything is serialized into a target-specific, compiled xmodel file. This xmodel is encrypted and then deployed on the FPGA using the runtime API through the embedded processor. We deploy the models on the Zynq-UltraScale+ MPSoC DPU architecture -DPUCZDX8L, seen Fig.8. The nomenclature refers to the target FPGA, quantization bit-width and design objective, with L being low latency. The DPU provides multiple configurations to trade off PL resources for performance. The B4096 core configuration yields the highest throughput with a peak of $18 \times 16 \times 16 \times 2 = 4096$ MAC/cycle. Three B4096-DPUCZDX8L cores can be deployed on the ZCU102.

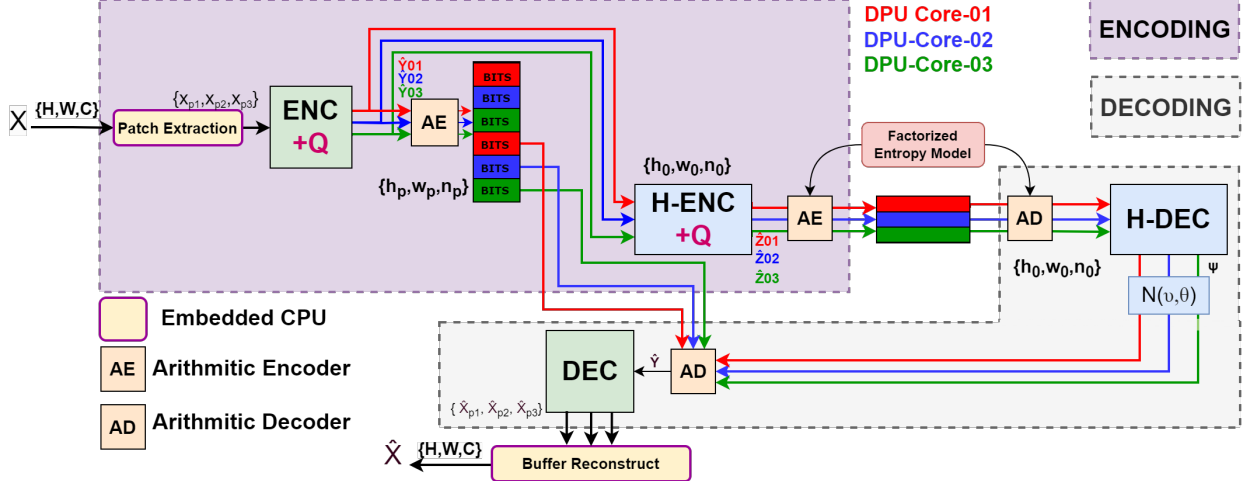


Fig. 7: Fully pipelined, patches are processed in parallel by three dedicated different computational cores, and intermediate outputs are available more quickly and passed immediately to the next module, this reduces the number of idle resources and utilizes the available bandwidth more efficiently.

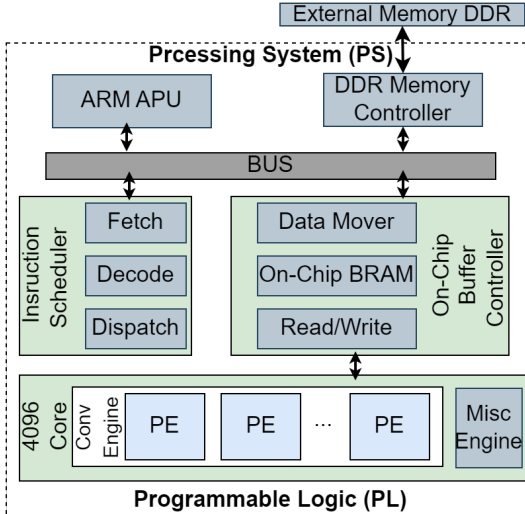


Fig. 8: Hardware architecture of the overall DPU

F. Analytical Model for Estimating FPS

This section introduces an analytical framework for estimating the Frames Per Second (FPS) of learned image compression (LIC) models deployed on the Vitis AI DPU 4096 accelerator. The framework provides a coarse-grained estimation of the model's performance before implementation, helping in the informed selection of model sizes to meet specific FPS targets. By integrating computational constraints and hardware parameters, the model offers a practical tool for hardware-aware model design.

The FPS of a model depends on the computational performance of the DPU core, as well as the model's workload, which is determined by the number of operations required to process a frame. The FPS can be estimated by calculating the time required to process one frame using the available compute power of the DPU.

The total frame time is mainly determined by the compute time, as memory transfer time is relatively negligible given the high bandwidth available and the small size of the data being processed. Thus, the FPS can be estimated as the inverse of the compute time.

The compute time is calculated as:

$$T_{\text{compute}} = \frac{N_{\text{workload}}}{\text{Peak Ops per Cycle} \times \eta}$$

Where:

- N_{workload} is the total number of operations required to process one frame.
- Peak Ops per Cycle is the total computational power available from the DPU cores.
- η is an efficiency factor accounting for any overhead, such as layer merging and memory caching inefficiencies.

The **Peak Ops per Cycle** is determined by the DPU configuration, which includes the number of input and output channels per layer, pixel parallelism, and core utilization. For each convolutional layer, the total number of operations per cycle per core is given by:

$$\text{Peak Ops per Cycle (per core)} = PP \times ICP \times OCP \times 2$$

Where:

- PP is the pixel parallelism, representing the number of pixels processed in parallel.
- ICP is the input channel parallelism, representing the number of input channels processed in parallel.
- OCP is the output channel parallelism, representing the number of output channels processed in parallel.
- The factor of 2 accounts for both input-output and weight operations in the convolution process.

For the B4096 configuration, where $PP = 8$, $ICP = 16$, and $OCP = 16$, the peak operations per cycle per core is:

$$\text{Peak Ops per Cycle (per core)} = 8 \times 16 \times 16 \times 2 = 4096$$

Given three DPU cores operating in parallel, the total peak operations per cycle across all cores is:

$$\text{Peak Ops per Cycle (total)} = 3 \times 4096 = 12,288$$

The total frame time, T_{frame} , is thus:

$$T_{\text{frame}} = \frac{N_{\text{workload}}}{\text{Peak Ops per Cycle (total)} \times \eta}$$

Finally, the FPS is the inverse of the total frame time:

$$\text{FPS} = \frac{1}{T_{\text{frame}}}$$

Substituting the expression for T_{frame} , the FPS can be written as:

$$\text{FPS} = \frac{\text{Peak Ops per Cycle (total)} \times \eta}{N_{\text{workload}}}$$

The total memory load per inference pass on a given model, B_{load} , can be approximated by:

$$B_{\text{load}} = \sum_{l=1}^L (H_l W_l N_l \times \Delta_l + H_l W_l N_{l+1} \times \Delta_l + N_l N_{l+1} K^2 \times \Delta_l) \quad (5)$$

where:

- L : Total number of layers in the model.
- H_l, W_l : Height and width of the feature map in layer l .
- N_l : Number of channels (feature maps) in layer l .
- N_{l+1} : Number of channels (feature maps) in the next layer ($l+1$).
- K : Kernel size (assumes square kernels of size $K \times K$).
- Δ_l : Bit-width or precision of the parameters and activations in layer l , expressed in bits.

IV. EXPERIMENTS AND RESULTS

In this section we experiment with the methodology proposed in the previous section over the [3] LIC model. First, we train a teacher model, we use it to teach two different students and we deploy the three models on FPGA, evaluating the different rate-distortion-complexity our method can attain against state of the art references. Second, we ablate each element of our proposed methodology assessing its contribution to the overall performance.

A. Training the teacher and distilling the students

To start with, we train from scratch the LIC model [3] for validating our experimental setup using the setup described in the original paper. The model is trained using a randomized train/validate/test dataset split of the combined CLIC, DIV2K, a subset of the Open Images datasets over batches of 256x256 randomly cropped patches and using the four λ values and the hyperparameters in Table II. This model that we refer to as *Teacher* is then used to teach two different student models

with 160 and 128 filters per layer that we will refer to as *Student-160* and *Student-128*, respectively.

Next, the teacher and the students are evaluated on the Kodak dataset following the same procedure described in related works like [20].

First, 720p (1280x720) HD images are produced repeatedly tiling the Kodak images. The tiled image is split into overlapping 256x256 patches with 56x56 stride, each patch is independently encoded and decoded, and finally, the decoded patches are reassembled into the whole picture. While such operations introduce some overhead, they are needed for HD and above pictures because of the otherwise impractical memory and bandwidth footprint on the FPGA and the hardware engine's requirements for fixed size input.

TABLE III: Number of GOPS required to process a 720p input after structured pruning

Module	Teacher-192	Student-160	Student-128
$f(\mathbf{x}; \theta_e)$	281.8	106.1	77.4
$g(\hat{\mathbf{y}}; \theta_d)$	300.4	114.3	75.6
$g_{ep}(\cdot; \theta_{ep})$	0.025	0.0087	0.006
$f_h(\mathbf{y}; \theta_{he})$	179.9	179.9	179.9
$g_h(\hat{\mathbf{z}}; \theta_{hd})$	224.1	224.1	224.1
Total Main	582.2	220.5	153.1
Total Hyper	404.0	404.0	404.0
Total	986.2	624.5	557.1

Table III shows the number of floating point operations at inference time for each module in Fig. 2. Dropping about 16% of the teacher filters in Student-160 is enough to cut the computational complexity by a twofold factor; dropping a further 16% filters in Student-128 slashes the complexity to a fourth overall. The students are then fine-tuned as described in Sec. III-A to improve their RD performance. The teacher and the two distilled students are then pruned as in Sec. III-C, the parameters are quantized as in Sec. III-D, the GDN is implemented as in Sec. III-B, and the corresponding xmodels are compiled and individually ported to the ZCU102 FPGA for benchmarking.

B. Performance evaluation

Fig. 9 compares RD-efficiency (rate vs. distortion) and latency (where available) for our proposed method and multiple references benchmarked on a ZCU102 FPGA. As an upper bound, we report the RD curve of the original LIC model [3] on a NVIDIA Tesla K80 GPU. As lower bounds, we report the RD curves of the JPEG and JPEG2000 standards. All FPGA-implemented model show a significant drop in RD efficiency mainly due to quantization: similar drops are shared by any FPGA implementation in the literature.

Coming to the comparison between FPGA-based models, we take as a reference the state of the art Sun2024 [22]. While in the hardware LIC literature it is not unseen comparing codecs measuring the PSNR delta for some target bitrate, we will always compare pairs of RD curves through Bjontegaard metrics[35]. Our Teacher outperform Sun2024 in RD efficiency (-8.95% BD-rate savings and 0.48 BD-PSNR better image quality), yet it is far from the 25 FPS target latency and

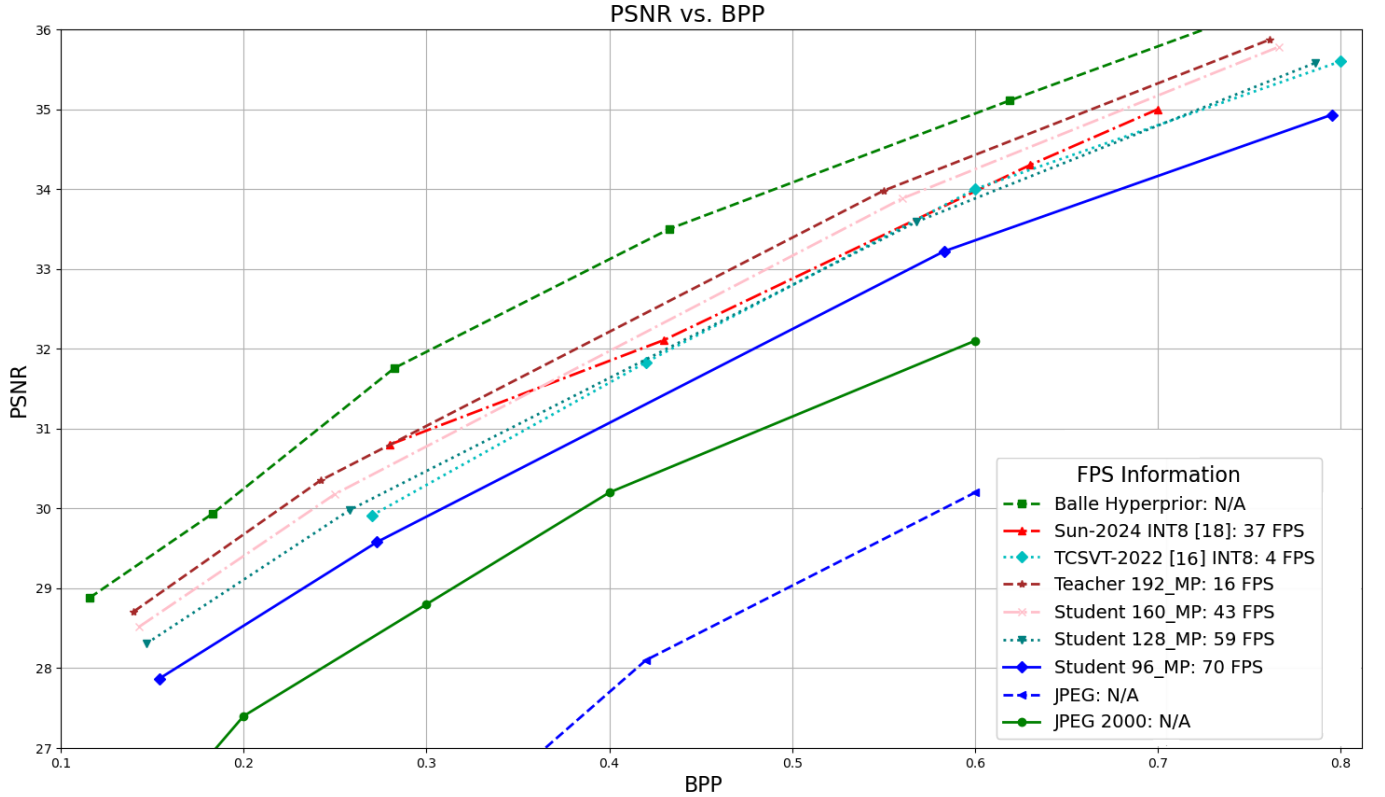


Fig. 9: Full R-D comparison with state of the art, [20], [22] and standard codecs on Kodak dataset

below the 37 FPS scored by Sun-2024. Student-160 achieves however better RD efficiency than Sun2024 (-5.32 BD-Rate savings and 0.25% better image quality), and also better latency (43 vs 37 FPS). Student-128 is in the chart because while it is less RD efficient than Sun2024 (+7.80% BD-Rate savings and -0.10% image quality), it meets the 50 FPS bar and is very close to the 60 FPS bar too.

Fig.10 shows the corresponding RD curves on the CLIC dataset [32] of the main 192K quantized and pruned hardware model compared to the corresponding float model and the original reference model by Ballé. The drop in RD from float to hardware is to be expected and is consistent throughout the experiments we have observed, pruning and fixed point quantization result in model degradation, this drop is minimized using fine tuning on both tasks.

Table. IV gives the encoding results comparison with the literature, our proposed implementation yields the highest frame rate results at 43 FPS compared to the 37 FPS stare of the art, we achieve the fastest hardware level encoding using a smaller FPGA board and DSP slices, in turn this results in our proposed implementation having the lowest energy/frame consumption at 2.88 F/frame. Despite these advancements, it is worth noting that [22] achieves a higher DSP utilization efficiency of 91% compared to our 85%. This difference can be attributed to their exhaustive design space exploration, which optimize DSP allocation across the pipeline. Nonetheless, the trade-off in our design prioritizes overall throughput, RD performance and energy efficiency , achieving a better balance for real-time encoding scenarios. These numbers show how

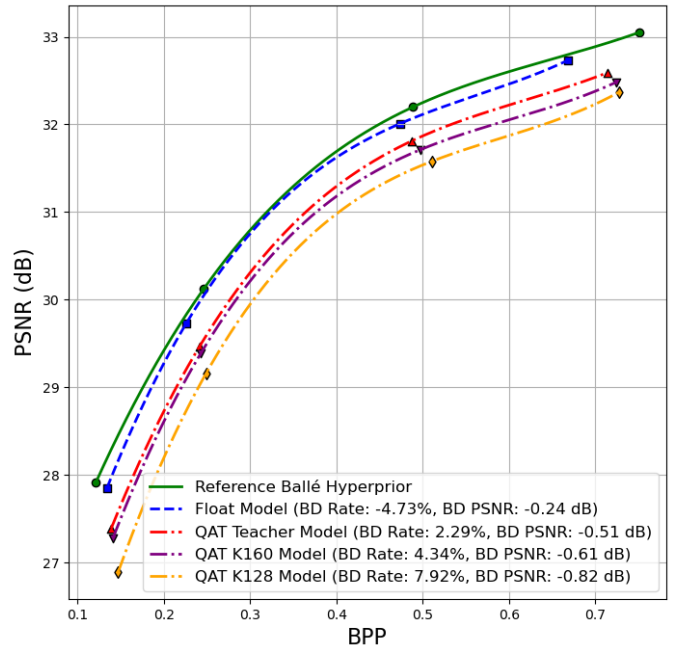


Fig. 10: RD plots and BD-rate, BD-PSNR results using Ballé model as reference on CLIC dataset.

our approach outperforms state-of-the-art competitors like [22] both in RD-efficiency and latency terms and without the need for a complex hardware design space search.

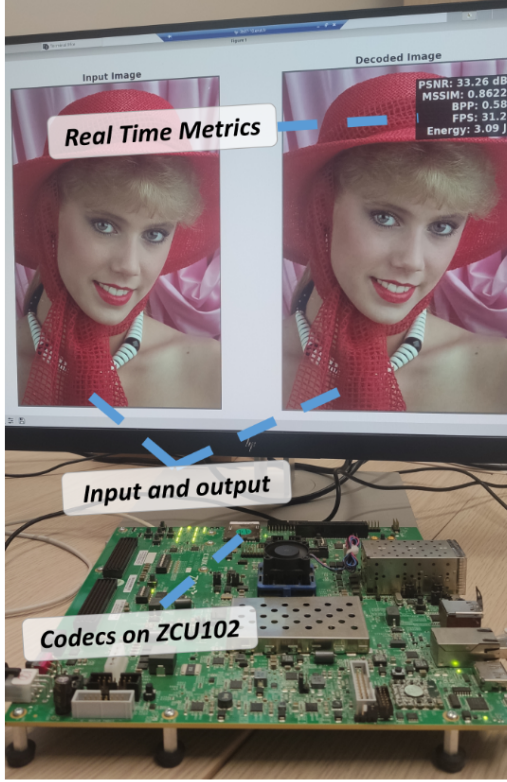


Fig. 11: ZCU102 FPGA setup during experimental validation showing real-time deployment on the embedded Linux

C. Analytical Model Validation

To validate the proposed analytical framework, we apply the model to three LIC models with different computational workloads and compare the estimated FPS with the observed FPS values.

We validate the analytical model with a set of experiments, using the ZCU102 FPGA with the following specifications:

- DPU frequency: 300 MHz
- DPU size: B4096, 3 cores in parallel, each capable of 4096 operations per cycle
- Memory bandwidth: 19.2 GB/s for PL and 19.2 GB/s for PS
- Input dimensions: $H = 1280, W = 720$
- Kernel size: $K = 5$

The workloads (in GOP/frame) for each model for the encoding task, after pruning, are as follows:

- 192K model: $\rightarrow 528.2$ GOP/frame
- 160K model: $\rightarrow 220.2$ GOP/frame
- 128K model: $\rightarrow 153.0$ GOP/frame

We also assume the following parameters:

- Peak operations per cycle (total): 12,288 operations per cycle (3 DPU cores, each capable of 4096 operations per cycle)

- Pipeline efficiency factor (η): 0.8 (Coarsely accounting for overhead of data transfer)

We test three different model configurations with varying numbers of channels (N):

$$N = 192, 160, 128$$

For each model, we compute the FPS based on the workload and the given parameters.

- a) *Model 192K (528.2 GOP/frame):* :

$$\text{FPS} = \frac{12,288 \times 0.8}{528.2} \approx 18.6$$

- b) *Model 160K (220.2 GOP/frame):* :

$$\text{FPS} = \frac{12,288 \times 0.8}{220.2} \approx 44.6$$

- c) *Model 128K (153.0 GOP/frame):* :

$$\text{FPS} = \frac{12,288 \times 0.8}{153.0} \approx 64.1$$

The FLOPs for each model are computed using the equation for $\text{FLOPs}_{\text{model}}$ based on the number of channels. The memory load is calculated using the memory traffic equation, and the FPS is estimated using the formulas described in earlier. The final FPS values are summarized in Table V.

1) *Discussion:* The analytical model provides a reasonable estimate of FPS across configurations, with deviations of around 12%. It effectively captures the transition from compute-bound performance at higher N values to memory-bound performance at lower N . For instance, at higher N values, the performance is primarily determined by the computational resources available in the DPU cores, while at lower N values, memory bandwidth plays a larger role. The framework allows users to select the number of channels (N) to meet rough FPS targets. For example, to achieve an FPS target of approximately 40, the model suggests $N = 160$, balancing both computational and memory demands. For FPS greater than 60, reducing N to 128 or less can minimize computational and memory requirements while still meeting throughput goals. However, we can see that for lower-load models like the 128K configuration, there is a greater discrepancy between the predicted and observed FPS. This is likely due to the fact that at lower N , the model approaches its memory limit, which hinders performance but is not accurately accounted for in the analytical model. Smaller models might be expected to improve throughput by utilizing more available resources, but in reality, performance is constrained by memory bandwidth at lower model sizes, resulting in memory-bound performance. Despite sufficient computational resources, the model cannot fully exploit them due to memory bandwidth limitations. Thus, while the analytical model suggests that reducing model size (lower N) alleviates computational load, this is not always the case when memory bandwidth becomes the limiting factor, leading to discrepancies, especially in low-computation configurations. The proposed analytical model offers a useful FPS estimate but simplifies key factors like memory access patterns, cache behavior, and intra-layer parallelism. It also doesn't fully account for the dynamic interaction between

TABLE IV: Hardware System Level Comparisons with the State of the Art

	Clock (MHz)	Encoding FPS ↑	DSP Usage	DSP Efficiency ↑	Energy (J/frame) ↓
ZCU102 (ours)	300	43.6	2148	85%	2.88
ZCU104 [20]	300	3.90	NA	NA	3.51
KU115 [21]	200	30.28	3706	54%	2.95
KU115 [22]	NA	37.74	4160	91.7%	NA

TABLE V: Validation of Analytical Model for Encoding-Only Pruned Models

N	GFLOPs	Predicted FPS	Observed FPS	Δ FPS ↓
192K	582.2	18.6	15.6	-16.13%
160K	220.2	44.6	43.1	-3.36%
128K	153.0	64.1	58.7	-8.42%

memory bandwidth and compute resources or factors like resource contention and synchronization delays. These aspects require detailed, cycle-level analysis similar to [15] which we leave for future work.

D. Ablation Study

In the next section, we study the contribution of each component of our architecture through ablation: since Student-160 shows the best RD efficiency while meeting the 25 FPS latency target, we will focus on this model from now on. We perform an ablation study where we independently drop from our architecture the knowledge distillation part, our GDN implementation, the mixed precision quantization, the quantization aware training, and the fully pipelined hardware configuration. For each ablated component, we assess the drop in RD efficiency, latency and resource utilization.

1) *Knowledge Distillation*: To start with, we assess the effect of the loss terms in Eq. 1 on the RD-efficiency of the knowledge distillation process. To this end, we fine-tune the K128 model and train it with 1) $\mathcal{L}_{\text{latent}}$ and $\mathcal{L}_{\text{perc}}$ KD losses 2) with only $\mathcal{L}_{\text{latent}}$ 3) only $\mathcal{L}_{\text{perc}}$ loss and finally with neither loss. Fig. 12 shows that not using the latent space loss results in an 11.62% increase in BD-Rate and a trivial drop in PSNR as the latent space loss typically helps guide the compressed representation of the student model (the learned latent representation) to be closer to that of the teacher model. This encourages the student model to learn better compression by distilling high-level information from the teacher, improving the rate (bitstream size). Whereas The output space loss focuses on the quality of the reconstructed image. It ensures that the student’s output (reconstructed image) closely matches the teacher’s output, guiding it to produce higher fidelity reconstructions with lower computational cost. As such, the absence of the outputs space loss results in a 0.36 dB drop in PSNR. Removing the entirety of the KD learning scheme results in a considerable loss in performance with a 25% increase in bpp and a significant drop of approximately 1 dB in PSNR compared to only +14% bpp and -0.3 dB with KD as seen in Fig.15. This demonstrates the essential role of both latent space and output space knowledge distillation losses in enhancing the performance of the student model. The significant increases in BD-rate and decreases in

PSNR observed in their absence underscore the importance of these losses in achieving efficient compression and high-quality reconstruction. These findings affirm that incorporating knowledge distillation is vital for bridging the performance gap between smaller models and their larger counterparts, ultimately leading to the desired RD and FPS targets.

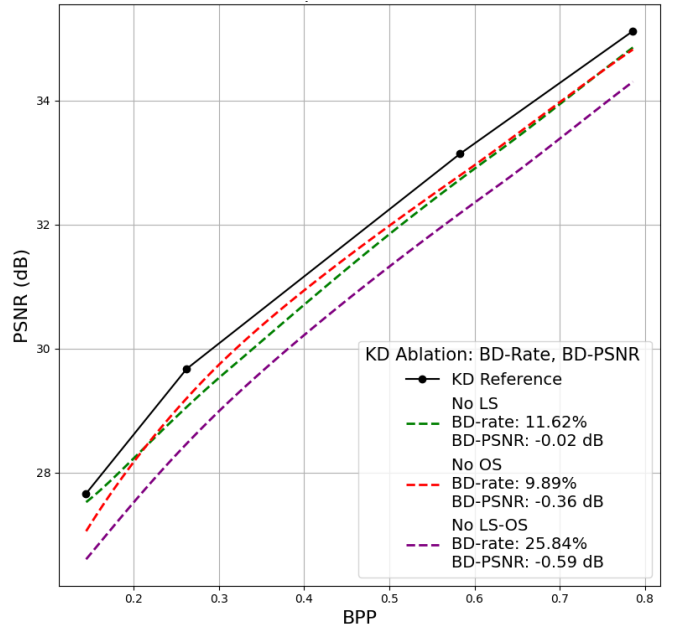


Fig. 12: BD-rate and BD-PSNR results for Latent Space and Output Space ablation showing a 0.6 PSNR drop and 25% rate increase when the KD protocol is not applied

2) *GDN vs ReLU*: Next, we drop our GDN implementation in favor of a simpler ReLU activation, as in [20], [22], [21]. While a drop in RD efficiency is expected [31], our work is the first to quantitatively assess it on an FPGA platform as we are the first to propose a GDN implementation on FPGA. Fig. 13 provides a better look into the difference in performance when using GDN instead of ReLU, in general an average drop of between -0.5 and -0.7 dB BD-PSNR and increase +10% and 25% BD-rate is observed throughout the different permutations, this goes in line with the insights gleaned in [31]. Therefore our GDN implementation pushed the RD-efficiency of our method by a significant margin giving our hardware LIC model the edge over the state of the art [22].

3) *Quantization strategy*: As a third set of ablation experiments, we experiment with two different aspects of the quantization strategy.

a) *Mixed Precision vs Single Precision*: As a first experiment, instead of allocating 32 rather than 8 bits to the GDN parameters to boost its precision (mixed precision), we allocate 8 bits

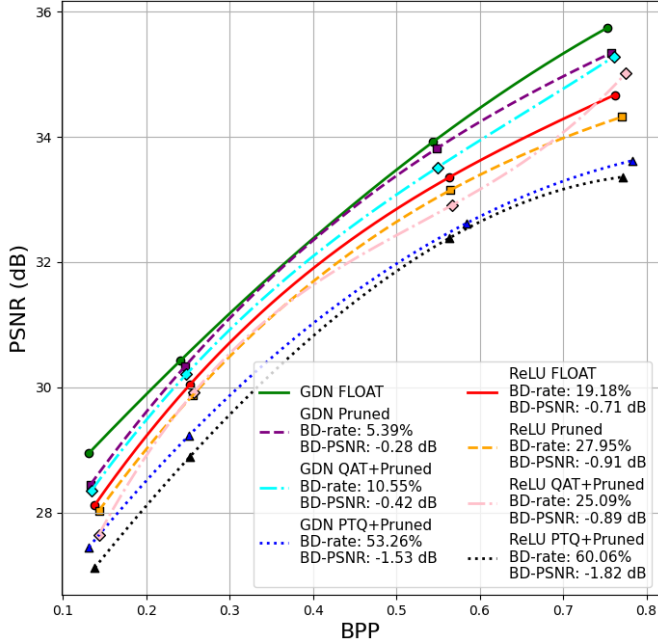


Fig. 13: BD-Rate and BD-PSNR results for several model permutations with a float model using GDN as reference

to all layers, i.e. we implement a single precision quantization scheme.

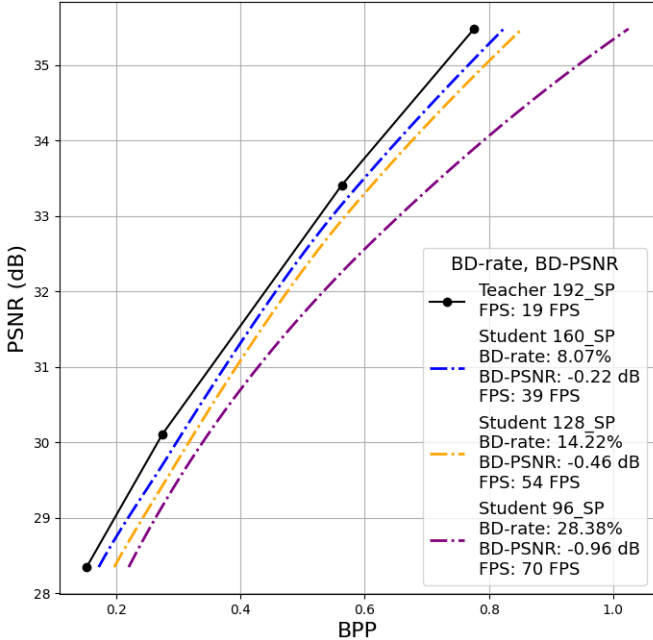


Fig. 14: BD rate and PSNR for Single Precision models

Tables. VII and VI highlight the difference in RD performance due to mixed precision quantization, assigning higher precision representation to the quantization error sensitive GDN activation layers results in consistent improvement in PSNR with an average of approximately +0.3 dB across all model permutations. Fig. 15 and 14 better highlight the advantage of using hybrid quantization, a change of approximately +0.3 dB PSNR and - 7% BPP can be observed, the margin

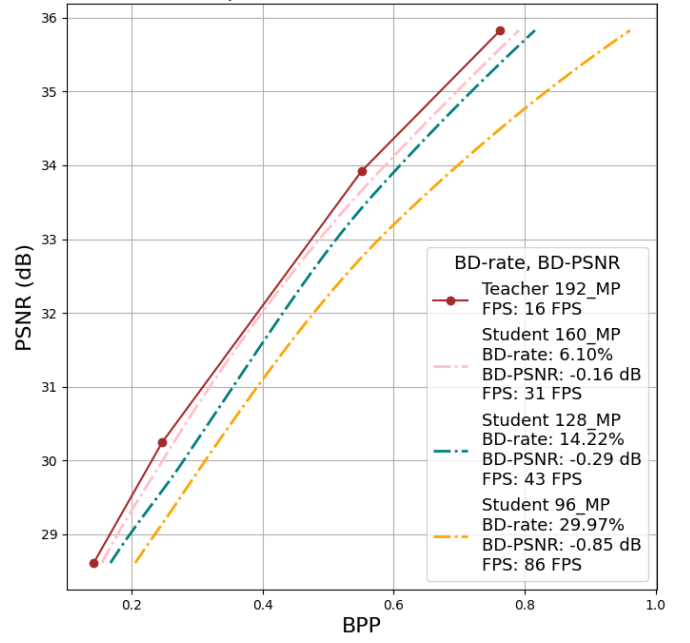


Fig. 15: BD rate and PSNR for Mixed Precision models

of improvement is thinner for smaller student models, this is likely due to the model's inability to properly capitalize on the higher precision representation because of its lower number of input and output channels per layer.

b) QAT vs. PTQ Quantization: Next, we replace Quantization Aware Tuning where quantization is followed by tuning for a simpler Post Training Quantization (PTQ) scheme where the model is quantized post-training without any further fine-tuning. Fig. 13 shows the RD curves for both quantization schemes: PTQ entails a large RD efficiency drop that we measured in a 40% BD-rate and a -1 dB BD-PSNR penalties. This experiment illustrates the benefits of integrating the quantization step in the learning loop when a multi-loss function is minimized at training time.

4) *Sequential vs Pipelined*:: Next, we assess the impact of our fully pipelined implementation in terms of latency over a simpler sequential configuration. We recall that our hardware design is fully pipelined as seen in Fig. 7, allowing parallel operations to occur simultaneously and taking full advantage of the three DPU cores. In contrast, other implementation in the literature in [20] use a unified computational lane that takes advantage of all available resources, leading to inefficiencies in bandwidth and resource utilization as a result of idle resources. Therefore, we experiment with a baseline sequential configuration where all model components (main encoder, hyperprior encoder, entropy encoder-decoder, hyperprior decoder, and main decoder) are executed one after another. This approach allows each component to utilize all available DPU cores for its specific task, yet at the cost of sub-optimal resource utilization due to idle resource usage within intermediate stages, leading to inefficiencies. Namely, a unified computational lane is dedicated to all processes, each module is processed individually and intermediate results are saved in the external memory and fetched when needed, all resources

TABLE VI: Single Precision KD Distillation Results on Kodak 720p Inputs

Lambda	Teacher K192		Student K160		Student K128		Student K96	
	Rate [bpp] ↓	PSNR [dB] ↑						
0.0016	0.152	28.35	0.136	28.22	0.144	27.66	0.151	27.29
0.0032	0.274	30.21	0.243	29.82	0.262	29.67	0.287	28.77
0.0075	0.563	33.41	0.573	33.35	0.583	33.14	0.612	32.66
0.0450	0.776	35.48	0.758	35.18	0.786	35.12	0.797	34.11

TABLE VII: Mixed Precision KD Distillation Results on Kodak 720p Inputs

Lambda	Teacher K192		Student K160		Student K128		Student K96	
	Rate [bpp] ↓	PSNR [dB] ↑						
0.0016	0.142	28.61	0.134	28.52	0.137	28.31	0.148	27.77
0.0032	0.247	30.25	0.223	30.18	0.232	29.98	0.263	29.48
0.0075	0.551	33.92	0.531	33.88	0.563	33.79	0.603	33.22
0.0450	0.763	35.83	0.724	35.78	0.766	35.68	0.785	34.73

TABLE VIII: Model latency as a function of the implementation configuration for a single 720p image.

Component	Sequential			Pipelined		
	FPS ↑	DSP Efficiency ↑	Avg Bandwidth	FPS ↑	DSP Efficiency ↑	Avg Bandwidth
Encoder	6.57	48%	4.9 GB/s	15.6	85%	10.8 GB/s
Decoder	4.27	45%	4.2 GB/s	11.7	68%	7.7 GB/s
Both	2.58	59%	6.8 GB/s	8.09	88%	9.6 GB/s

TABLE IX: Model latency as a function of the implementation configuration for a single 720p image on the 160K student.

Component	Sequential			Pipelined		
	FPS ↑	DSP Efficiency ↑	Avg Bandwidth	FPS ↑	DSP Efficiency ↑	Avg Bandwidth
Encoder	10.1	56%	3.5 GB/s	43.6	87%	7.1 GB/s
Decoder	6.5	51%	3.3 GB/s	15.5	75%	6.7 GB/s
Both	3.8	59%	3.7 GB/s	22.1	81%	8.5 GB/s

are available to whatever module is being run. Tables.VIII gives system level performance numbers for the mapped K192 teacher model using both design space configurations, the fully pipelined configuration results in higher DSP efficiency and external memory bandwidth which translate into a x2.5 FPS performance. In Table IX, the 160K student model, distilled via knowledge distillation, demonstrates significantly higher performance. KD reduces the model size, directly lowering the number of floating-point operations (FLOPs) required for inference. This reduction in computational load results in higher memory bandwidth (10.8 GB/s in the pipelined encoder) and improved DSP efficiency (87%) by allowing a more efficient utilization of available hardware resources on the ZCU102 FPGA. As a result, the student model achieves 42.6 FPS in the pipelined encoder, nearly 3x faster than the sequential model. The exploration of FPGA engine design reveals that the fully pipelined configuration offers substantial performance benefits compared to the sequential approach. By leveraging parallel processing and optimizing resource allocation, the pipelined setup fully exploits the capabilities of the ZCU102 FPGA.

V. CONCLUSION AND FUTURE WORKS

This work presents a hardware-efficient FPGA implementation of a Learned Image Compression (LIC) model, achieving real-time latency while maintaining high RD-efficiency. A novel transfer learning scheme is introduced, enabling the use

of larger models while reducing computational requirements. Another contribution to the design is a custom Generalized Divisive Normalization (GDN) layer optimized for FPGA, significantly enhancing rate-distortion (RD) performance. A mixed-precision approach, using 32-bit precision for the GDN layer and 8-bit for the remaining layers, provides an optimal trade-off between resource usage and RD performance. This results in an average PSNR gain of 0.8 dB and a 7% reduction in bit-rate, with the GDN layer requiring just 4% of total model FLOPS. Additional optimizations through Quantization-Aware Training (QAT) and structured pruning further reduce model size and complexity without significantly impacting quality. QAT improves robustness to quantization, yielding a 40% BD-rate improvement and a 1 dB PSNR gain over standard Post-Training Quantization (PTQ). Structured pruning eliminates up to 30% of model parameters, enhancing resource efficiency and throughput on FPGA. These enhancements enable real-time performance, reaching 43 FPS on 720p inputs, while surpassing state-of-the-art RD metrics. Finally, our fully pipelined FPGA design maximizes resource utilization, delivering up to 3x the performance of sequential designs and closely matching floating-point reference models, thus outperforming other FPGA-based approaches in the literature. Future work will extend the knowledge distillation scheme to cross-architectural KD, leveraging the strong RD performance of vision transformers while distilling their knowledge into more efficient convolutional neural network autoencoder-based

architectures. We also plan to refine the KD scheme to account for gradual dynamic weighting instead of discrete phases, and expand the tests to include the hyperprior model with the aim of improving the entropy performance of the student model. On the hardware side, we plan to explore low-level design space exploration using analytical and experimental software-hardware co-modeling to optimize mapping configurations.

REFERENCES

- [1] G. Lu, X. Ge, T. Zhong, Q. Hu, and J. Geng, “Preprocessing enhanced image compression for machine vision,” *IEEE Transactions on Circuits and Systems for Video Technology*, vol. 34, no. 12, pp. 13 556–13 568, 2024.
- [2] J. Ballé, V. Laparra, and E. Simoncelli, “End-to-end optimized image compression,” in *Proc. Int. Conf. Learn. Represent.* ICLR.
- [3] J. Ballé, D. Minnen, S. Singh, S. Hwang, and N. Johnston, “Variational image compression with a scale hyperprior.”
- [4] D. Minnen, J. Ballé, and G. Toderici, “Joint autoregressive and hierarchical priors for learned image compression,” in *Proc. Adv. Neural Inf. Process. Syst.* pp. 10 771–10 780.
- [5] T. Chen, H. Liu, Z. Ma, Q. Shen, X. Cao, and Y. Wang, “End-to-end learnt image compression via non-local attention optimization and improved context modeling,” vol. 30, pp. 3179–3191.
- [6] A. B. Koyuncu, P. Jia, A. Boev, E. Alshina, and E. Steinbach, “Efficient contextformer: Spatio-channel window attention for fast context modeling in learned image compression,” *IEEE Transactions on Circuits and Systems for Video Technology*, vol. 34, no. 8, pp. 7498–7511, 2024.
- [7] J. Lee, S. Cho, and S.-K. Beack, “Context-adaptive entropy model for end-to-end optimized image compression.”
- [8] Z. Cheng, “Learned image compression with discretized gaussian mixture likelihoods and attention modules,” in *Proceedings of the IEEE/CVF conference on computer vision and pattern recognition*. CVPR, Jun, pp. 7939–7948.
- [9] J. Ballé, “Efficient nonlinear transforms for lossy image compression,” in *2018 Picture Coding Symposium (PCS)*. IEEE, 2018, pp. 248–252.
- [10] Y. Wu, X. Li, Z. Zhang, X. Jin, and Z. Chen, “Learned block-based hybrid image compression,” *IEEE Transactions on Circuits and Systems for Video Technology*, vol. 32, no. 6, pp. 3978–3990, 2022.
- [11] A. Mazouz and C. P. Bridges, “Automated offline design-space exploration and online design reconfiguration for cnns,” in *2020 IEEE Conference on Evolving and Adaptive Intelligent Systems (EAIS)*, 2020, pp. 1–9.
- [12] J. Fowers, G. Brown, P. Cooke, and Stitt, “G.: A performance and energy comparison of FPGAs, GPUs, and multicores for sliding window applications,” in *Proceedings of the ACM/SIGDA international symposium on Field Programmable Gate Arrays*.
- [13] F. Gan, H. Zuyi, C. Song, and W. Feng, “Energy-efficient and high throughput FPGA-based accelerator for convolutional neural networks,” in *2016 13th IEEE International Conference on Solid-State and Integrated Circuit Technology (ICSICT)*, pp. 624–626.
- [14] S. Choi, J. Sim, M. Kang, and L.-S. Kim, “TrainWare: a memory-optimized weight update architecture for on-device convolutional neural network training,” in *Proceedings of the International Symposium on Low Power Electronics and Design*.
- [15] A. Mazouz and C. P. Bridges, “Automated CNN back-propagation pipeline generation for FPGA online training,” vol. 18, pp. 2583–2599. [Online]. Available: <https://doi.org/10.1007/>
- [16] ———, “Adaptive hardware reconfiguration for performance tradeoffs in CNNs,” in *2019 NASA/ESA Conference on Adaptive Hardware and Systems (AHS)*, 2019, pp. 33–40.
- [17] H. Cheng, M. Zhang, and J. Q. Shi, “A survey on deep neural network pruning-taxonomy, comparison, analysis, and recommendations.”
- [18] C. M. J. Tan and M. Motani, “Dropnet: Reducing neural network complexity via iterative pruning,” in *International Conference on Machine Learning. PMLR*.
- [19] A. Gholami, *A survey of quantization methods for efficient neural network inference*. Low-Power Computer Vision. Chapman and Hall/CRC.
- [20] C. Jia, X. Hang, S. Wang, Y. Wu, S. Ma, and W. Gao, “FPX-NIC: An FPGA-accelerated 4k ultra-high-definition neural video coding system,” vol. 32, no. 9, pp. 6385–6399.
- [21] H. Sun, Q. Yi, F. Lin, L. Yu, J. Katto, and M. Fujita, “Real-time learned image codec on FPGA,” in *2022 IEEE International Conference on Visual Communications and Image Processing (VCIP)*, pp. 1–1.
- [22] H. Sun, Q. Yi, and M. Fujita, “Fpga codec system of learned image compression with algorithm-architecture co-optimization,” *IEEE Journal on Emerging and Selected Topics in Circuits and Systems*, 2024.
- [23] L. Theis, W. Shi, A. Cunningham, and F. Huszár, “Lossy image compression with compressive autoencoders.”
- [24] J. Ballé, V. Laparra, and E. P. Simoncelli, “Density modeling of images using a generalized normalization transformation,” *arXiv preprint arXiv:1511.06281*, 2015.
- [25] D. Minnen, J. Ballé, and G. D. Toderici, “Joint autoregressive and hierarchical priors for learned image compression,” *Advances in neural information processing systems*, vol. 31, 2018.
- [26] D. Minnen and S. Singh, “Channel-wise autoregressive entropy models for learned image compression,” 2020. [Online]. Available: <https://arxiv.org/abs/2007.08739>
- [27] R. Zou, C. Song, and Z. Zhang, “The devil is in the details: Window-based attention for image compression,” in *Proceedings of the IEEE/CVF conference on computer vision and pattern recognition*, 2022, pp. 17 492–17 501.
- [28] Z. Duan, M. Lu, Z. Ma, and F. Zhu, “Lossy image compression with quantized hierarchical values,” in *Proceedings of the IEEE/CVF Winter Conference on Applications of Computer Vision*, pp. 198–207.
- [29] Xilinx, “Xilinx vitis ai development environment, [online available: <https://www.xilinx.com/products/design-tools/vitis/vitis-ai.html>.]”
- [30] Y. Gao, B. Zhang, X. Qi, and H. K.-H. So, “DPACS: Hardware accelerated dynamic neural network pruning through algorithm-architecture co-design,” in *Proceedings of the 28th ACM International Conference on Architectural Support for Programming Languages and Operating Systems*, vol. 2. Association for Computing Machinery, pp. 237–251.
- [31] J. Ballé, N. Johnston, and D. Minnen, “Integer networks for data compression with latent-variable models,” in *Proc. Int. Conf. Learn. Represent.* pp. 1–17.
- [32] G. Toderici, L. Theis, N. Johnston, E. Agustsson, F. Mentzer, and J. Balle, “Wenzhe éshi, and radu timofte. clic 2020: Challenge on learned image compression.”
- [33] E. Agustsson and R. Timofte, “Ntire 2017 challenge on single image super-resolution: Dataset and study,” in *Proceedings of the IEEE conference on computer vision and pattern recognition workshops*.
- [34] A. Kuznetsova, “The open images dataset v4: Unified image classification, object detection, and visual relationship detection at scale,” vol. 128, no. 7, pp. 1956–1981.
- [35] G. Bjontegaard, “Calculation of average psnr differences between rd-curves,” *ITU-T SG16 Q*, vol. 6, 2001.